J. Nanoanalysis., 6(4): 275-288, Autumn 2019

ORIGINAL RESEARCH PAPER

Employing α-Fe_2O_3 /$Mn_2P_2O_7$ as a nano photocatalyst for degradation of toluene in aqueous environment

Sajjad Mafi, Kazem Mahanpoor*

Department of Chemistry, Arak Branch, Islamic Azad University, Arak, Iran

Received: 2019-03-17 Accepted: 2019-09-01 Published: 2019-09-20

ABSTRACT

In this study, α-Fe_2O_3 nano-spheres are immobilized on the surface of manganese pyrophosphate ($Mn_2P_2O_{7)}$ support using forced hydrolysis and reflux condensation (FHRC) method. The synthesized α-Fe_2O_3/$Mn_2P_2O_7$ were characterized by FTIR, SEM, BET EDX, and XRD. The photocatalytic activity from α-Fe_2O_3/$Mn_2P_2O_7$ was investigated for the removal of toluene in aqueous solution by UV/H_2O_2 system. The chemical oxygen demand (COD) measurements were used to determine the amount of toluene removal. The experiments were designed based on four affecting variables, including pH, catalyst content, initial toluene concentration and H_2O_2 at three levels using Box-Behnken experimental design. The results of this study showed that α-Fe_2O_3/$Mn_2P_2O_7$ as a new photocatalyst has a higher photocatalytic activity than α-Fe_2O_3 nanoparticles. Based on the achieved results, the maximum degradation efficiency was 97.14% in optimal conditions.

Keywords: *Manganese Pyrophosphate; Photocatalyst; α-Fe_2O_3 nanoparticles; Box-Behnken method; Toluene*

How to cite this article
*Mafi S, Mahanpoor K. Employing α-Fe_2O_3 /$Mn_2P_2O_7$ as a nano photocatalyst for degradation of toluene in aqueous environment. J. Nanoanalysis., 2019; 6(4): 275-288. DOI: 10.22034/jna.****

INTRODUCTION

The presence of various organic pollutants, especially volatile organic matter, including toluene in aquatic environments has become an important environmental issue in recent years [1-4]. The development of effective technologies to reduce and eliminate toxic and hazardous compounds in water and sewage is one of the issues that have been discussed globally [5-8]. One of the most important problems of water treatment methods is the inability to treat contaminants at low concentrations and toxic properties resistant to certain contaminants resistant to biological agents and cannot be easily decomposed [9-12].

Over the past decade, advanced oxidation processes (AOPs) proved to be the alternate method for removing recalcitrant, as well as nonbiodegradable compounds. One of the most important AOPs is a heterogeneous photocatalytic oxidation process with semiconductors such as hematite (α-Fe_2O_3) due to its high stability, non-toxic, environmentally friendly and corrosion-resistant nature [13-16]. However, one of the important issues in using catalysts, especially in nanoscale dimensions, is recycling and reuse. Fixing the catalyst on a suitable basis is one of the ways to solve this problem. Manganese pyrophosphate ($Mn_2P_2O_7$) has attracted much attention because of its versatile coordination modes, low toxicity, interesting magnetic property, catalyst in oxidative dehydrogenation of hydrocarbons and biocompatibility [17-18]. Therefore, here we used the manganese pyrophosphate in order for immobilization of the α-Fe_2O_3 nanoparticle. Forced Hydrolysis and Reflux Condensation (FHRC) techniques were used for the preparation of α-Fe_2O_3 / $Mn_2P_2O_7$ [19]. Characterization of the α-Fe_2O_3 / $Mn_2P_2O_7$ was carried out using Fourier transform infrared spectroscopy (FTIR), X-ray diffraction (XRD), Brunauer–Emmett–Teller (BET), scanning

* Corresponding Author Email: *k-mahanpoor@iau-arak.ac.ir*
k.mahanpoor@gmail.com

electron microscopy (SEM) and energy dispersive X-ray (EDAX) analysis. The performance of pure and supported α-Fe_2O_3 NPs on the Toluene photocatalytic degradation was investigated using Box-Behnken designs [20-22]. In this study, chemical oxygen demands (COD) reduction was also monitored in order to explain the degradation of toluene in the UV/nanocomposite system, and the optimal conditions were presented.

MATERIALS AND METHODS

Materials and instrument

All reagents were of analytical grade were purchased from Merck (Germany) company and used without further purification. A Philips XL30 scanning electron microscope system was used for morphological and elemental analysis. The Fourier-transform infrared spectroscopy (Perkin-Elmer, Spectrum two) was accomplished in the range of 400–4000cm^{-1}. XRD patterns were recorded by DX27-mini, X-ray diffractometer using Ni-filtered Cu Ka radiation (λ= 1.5406). The Chemical Oxygen Demands (COD) were measured by COD Meter and Multiparameter Photometer (Hanna-HI83214). The solution pH values were measured with a Metrohm 780 pH meter. The textural property was measured using N_2 adsorption-desorption isotherms method on the BET–BJH specific surface area measurement equipment (Micromeretics ASAP 2010 system).

Preparation of $Mn_2P_2O_7$

The manganese metal powder and P_2S_5 as the reaction precursors under solvothermal condition were used in order to synthesize manganese pyrophosphate species. In a conventional method, 0.002 mol of Mn and 0.002 mol of P_2S_5 were blended together and with 30 mL of ethylene glycol in a stainless steel autoclave (volume: 50 ml). The autoclave was sealed and heated for a period of 24-40 hours at 220 °C, then allowed to naturally cool to room temperature. The final pale pink precipitates were separated using centrifugation, completely rinsed with double distilled water and ethanol, and then dried at 60 °C using a vacuum oven. The following Eq. 1 represents the overall reaction [18]:

$$2Mn + P_2S_5 + 7HOCH_2CH_2OH \rightarrow Mn_2P_2O_7 + 7CH_3CHO + 5H_2S + 2H_2 \quad (1)$$

Synthesis of α-Fe_2O_3 /$Mn_2P_2O_7$ nano photocatalyst using FHRC

In the beginning, 50 ml of iron (III) chloride hexahydrate with a concentration of 0.25 M was entered into a beaker. Then, 4 g of synthesized $Mn_2P_2O_7$ compound was added gently under intense agitation. The obtained mixture was stirred for 4-5 hours. Afterward, stirring was stopped by the obtained solids to be settled. The segregated solid transferred into a 50ml flask. Then 50 ml of urea with a concentration of 1 M was slowly added to the solution when it was stirred in the flask. The obtained mixture was kept at 90 °C for 12 hours under reflux condition. In order to remove the unreacted ions, the resulting separated precipitate was washed out using a 1:1 solution of ethanol/ deionized water. The obtained product was stored at room temperature for 2 hours and then dried at 80 °C for 2 hours. Ultimately, the calcination of the product was done at 300 °C for 1 hour [19].

Box- Behnken design

A second-order polynomial Eq. 2 was used through nonlinear regression to fit the experimental data and to identify the relevant model terms. The quadratic response model can be as follows [23]:

$$Y = \alpha_0 + \sum_{i=1}^{k} \alpha_i x_i + \sum_{i=1}^{k} \alpha_{ii} x_i^2 + \sum \sum_{i<j} \alpha_{ij} x_i x_j + \varepsilon \quad (2)$$

Where α_0 is the constant, α_i the slope or linear effect of the input factor x_i, α_{ij} the linear-by-linear interaction effect between the input factors xi and x_j, and α_{ii} is the quadratic effect of input factor *xi* and ε is the residual error.

The experimental range and variables levels have been listed in Table 1. pH varied from 5 to 9 (5, 7 and 9), the initial concentration of toluene from 100 to 200 ppm (100, 150 and 200 ppm), catalyst concentration from 60 to 120 ppm (60, 90 and 120 ppm) and H_2O_2

Table 1. Experimental range and levels of the variables.

Independent variables	Range of levels		
pH	5	7	9
H_2O_2 con. (ppm)	0.1	0.3	0.5
Catalyst con. (ppm)	60	90	120
Initial con. of toluene (ppm)	100	150	200

initial concentration from 0.1 to 0.5 ppm (0.1, 0.3 and 0.5 ppm). The 27 experiments related to this Box-Behnken design and their experimental conditions have been listed in Table 2. The experiments 25, 26, and 27 were repeated to increase the accuracy of the results. The removal efficiency of toluene was a dependent response. In order to do DoEs, Minitab 16 version 16.2.0 statistical software was utilized. In addition, an analysis of variance (ANOVA) was run to analyze the results.

General procedure for photocatalytic degradation of toluene

In order to carry out each experiment (according to Table 2), firstly 250 ml toluene solutions were made as specified concentration and poured inside the reactor. The photocatalytic degradation of pollutants, according to the Eq. 3 was calculated as a function of time:

$$X\,\% = \frac{COD_0 - COD_t}{COD_0} \times 100 \text{ QUOTE } X\% = \frac{C_0 - C_t}{C_0} \times 100 \; X\% = \frac{C_0 - C_t}{C_0} \times 100 \quad (3)$$

Where the COD of toluene solution to the start of the photocatalytic process (t = 0) is COD_0 and after a time t is COD_t. Fig. 1 shows one schematic picture of photocatalytic reactor used in the work. In an MDF box was placed a glass reactor with a magnetic stirrer, UV irradiation was done from the top of the reactor and sampling was done using a syringe.

RESULTS AND DISCUSSION

Catalyst characterization

The SEM images of $Mn_2P_2O_7$ and α-Fe_2O_3 / $Mn_2P_2O_7$ are shown in Fig. 2. As shown in SEM image Fig. 2 (B), nanoparticles of α-Fe_2O_3 were quasi-spherically supported on the surface of $Mn_2P_2O_7$. Creation of spherical structures of separate and independent boundaries can be observed that can have a relatively high effective level. These structures have a fairly uniform size distribution. The quasi-spherical particles of α-Fe_2O_3 synthesized in the FHRC method are denser and are less distant from each other on the base of the catalyst.

Table 2. The toluene removal percentage under various experimental conditions.

Exp. no.	Variables				Toluene removal (X %)	
	PH	H_2O_2 con. (ppm)	Catalyst con. (ppm)	Toluene initial con. (ppm)	Pure α-Fe_2O_3	α-Fe_2O_3 / $Mn_2P_2O_7$
1	5	0.1	90	150	50.22	62.89
2	9	0.1	90	150	52.13	68.37
3	5	0.3	90	150	54.67	70.56
4	9	0.5	90	150	62.34	75.80
5	7	0.3	60	100	73.18	78.55
6	7	0.3	120	100	84.32	95.23
7	7	0.3	60	200	39.45	44.07
8	7	0.3	120	200	68.33	50.99
9	5	0.3	90	100	81.42	77.28
10	9	0.3	90	100	78.57	90.47
11	5	0.3	90	200	40.87	45.78
12	9	0.3	90	200	35.43	42.48
13	7	0.1	60	150	53.36	65.51
14	7	0.5	60	150	50.43	61.45
15	7	0.1	120	150	61.78	74.25
16	7	0.5	120	150	72.47	82.83
17	5	0.3	60	150	50.26	67.73
18	9	0.3	60	150	54.67	65.09
19	5	0.3	120	150	64.41	76.18
20	9	0.3	120	150	73.57	83.55
21	7	0.1	90	100	62.52	70.05
22	7	0.5	90	100	79.57	90.12
23	7	0.1	90	200	37.65	43.02
24	7	0.5	90	200	35.78	38.98
25	7	0.3	90	150	62.13	74.81
26	7	0.3	90	150	62.55	74.26
27	7	0.3	90	150	62.12	74.94

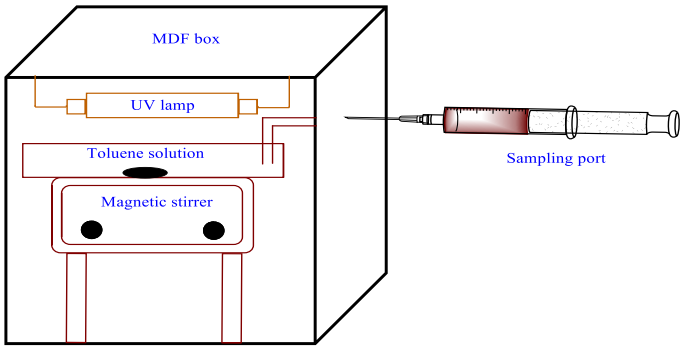

Fig. 1. Schematic picture of the photocatalytic reactor.

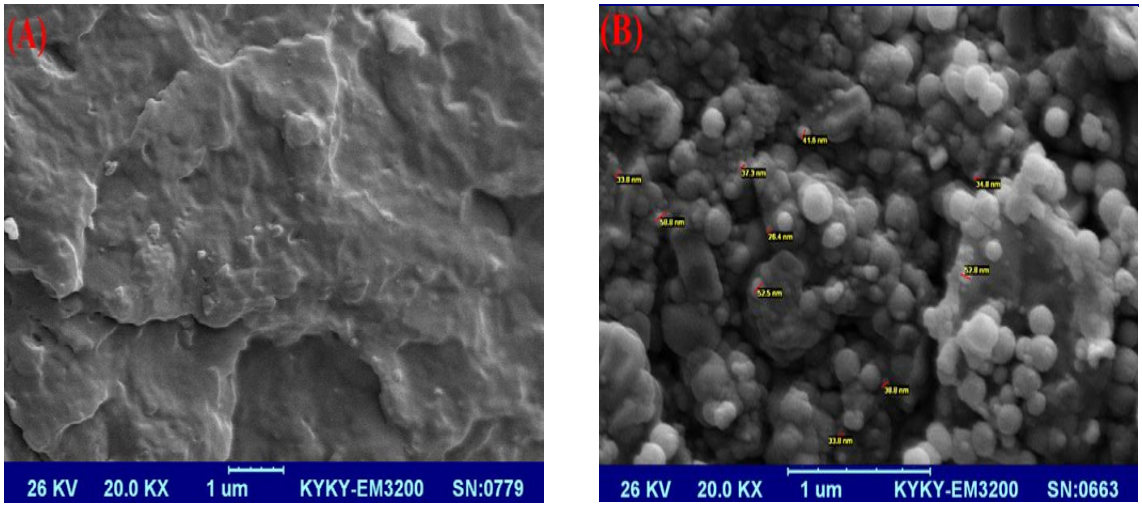

Fig. 2. SEM image of the synthesized $Mn_2P_2O_7$ (A), and α-Fe_2O_3 /$Mn_2P_2O_7$ by FHRC method (B).

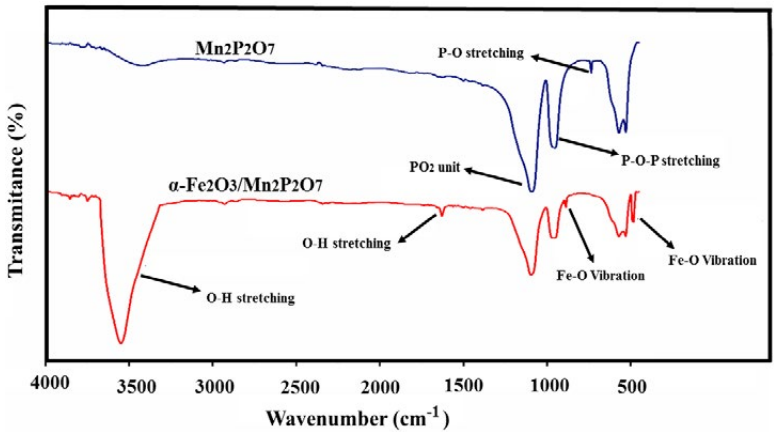

Fig. 3. The FTIR spectra of catalyst support of $Mn_2P_2O_7$ and α-Fe_2O_3/ $Mn_2P_2O_7$.

The FTIR spectra of pristine $Mn_2P_2O_7$ and synthesized α-Fe_2O_3/$Mn_2P_2O_7$, which were prepared using the FHRC method, are shown in Fig. 3. In the FTIR spectrum of synthesized $Mn_2P_2O_7$, the strong vibrating band at 1094 cm^{-1} is related to asymmetric stretching of PO_2 unit. The peaks at 736 cm^{-1} and 950 cm^{-1} are corresponded to stretching vibration of P-O bond and symmetric or asymmetric stretching mode of P-O-P tertiary group, respectively. The FT-IR spectrum of α-Fe_2O_3/$Mn_2P_2O_7$ composite showed the bands at 1600 cm^{-1} and 3500 cm^{-1} due to bending and stretching vibrating modes of O-H

bond, respectively. The peaks at around 482 cm^{-1} and 886 cm^{-1} are related to the vibration of Fe-O bond. Other changes in the spectral range from 400 to 500 cm^{-1} represents the formation of new bonds between α-Fe_2O_3 and $Mn_2P_2O_7$ [24- 25].

The PXRD patterns of the synthesized $Mn_2P_2O_7$, α-Fe_2O_3 and α-Fe_2O_3/$Mn_2P_2O_7$ compounds are shown in Fig. 4. In the pattern of α-Fe_2O_3/$Mn_2P_2O_7$ composite, the Bragg reflections of (111), (-201), (130), (131) and (-311) can be observed at 2θ = 28.96°, 30.36°, 34.41°, 41.61° and 43.71°, respectively, which were in good agreement with powder diffraction data of the monoclinic structure of $Mn_2P_2O_7$ [18]. Moreover, some extra peaks at 2θ = 24.11, 33.06°, 35.66°, 49.26° and 54.01° which were attributed to the planes of (012), (104), (110), (024) and (116) in the rhombohedral (hexagonal) structure of α-Fe_2O_3 (space group: *R*-3*c*), were observed in the XRD pattern of the synthesized α-Fe_2O_3/$Mn_2P_2O_7$ composite [26].

To determine the specific surface area of the α-Fe_2O_3/$Mn_2P_2O_7$ composite and pristine $Mn_2P_2O_7$, the BET method has been used. Fig. 5 shows the obtained isotherms of the aforementioned compounds. The observed hysteresis loop in the obtained adsorption-desorption isotherms of these materials classified as type IV by IUPAC. The measured specific surface area of the solid support was 125 m^2/g. After the formation of the composite, the surface area was increased to 160 m^2/g. The observed change in the surface area is arising from the presence of the α-Fe_2O_3 nanoparticles on the surface of $Mn_2P_2O_7$ support.

In this study, EDAX method was used to determine the presence and the elements amount in the synthesized composite. The obtained EDAX spectrum of the synthesized composite is shown in Fig.6. Based on the obtained results from the

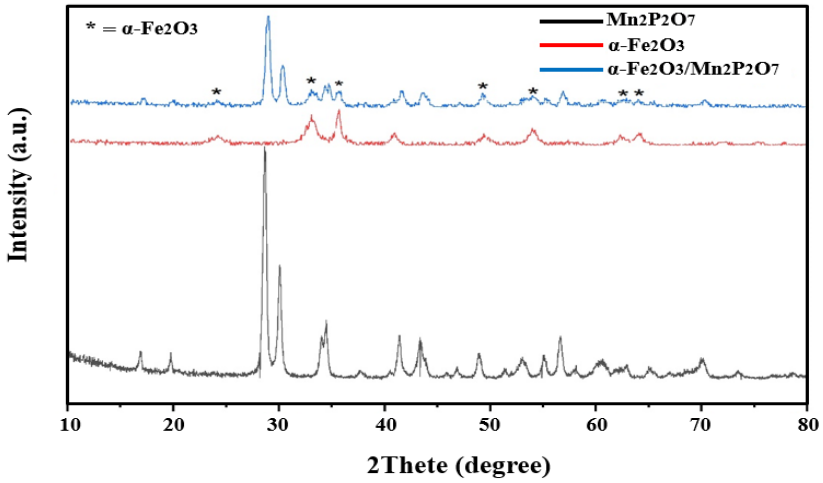

Fig. 4. The XRD patterns of the synthesized compounds.

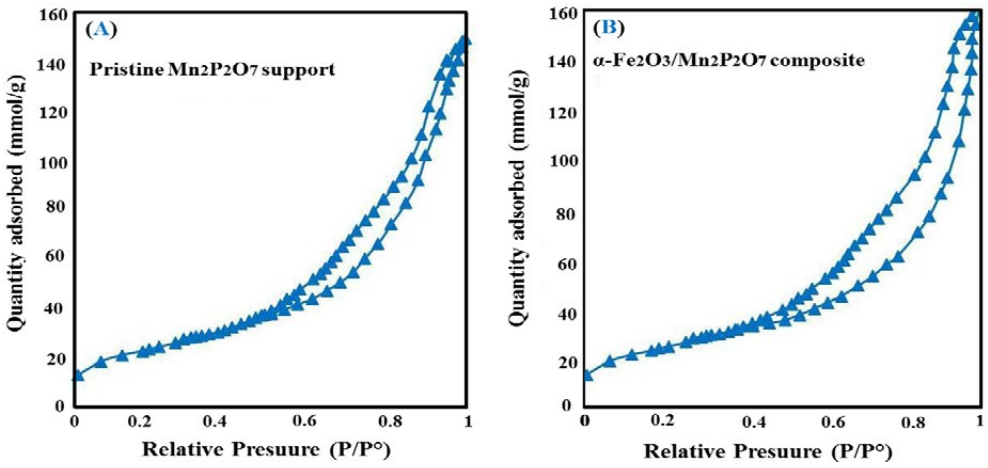

Fig. 5. Adsorption-desorption isotherms of (A) synthesized $Mn_2P_2O_7$ and (B) α-Fe_2O_3/$Mn_2P_2O_7$ composite.

spectrum, the presence of oxygen, phosphorus, iron and manganese elements in the synthesized composite was confirmed. Based on the results, it can be concluded that α-Fe_2O_3/$Mn_2P_2O_7$ composite was formed.

In Table 2, experiments data were reported in the 100 minutes based on the performed the toluene removal percentages. In general, the comparison of the removal results showed that the amount of toluene degradation in pure nanoparticles was less than that of the nanoparticles immobilized on the support. These results show that the addition of support to the nanoparticles has increased their photocatalytic activity.

The photocatalytic process essentially relates to the absorption and excretion of molecules on the catalyst surface, after irradiation of the α-Fe_2O_3 /$Mn_2P_2O_7$ with UV light, the electrons of the valence band (VB) of the catalyst are driven to the conductive band (CB) and the cavities are produced in the valence band.

The produced cavities can react with adsorbed water on the surface of the α-Fe_2O_3 /$Mn_2P_2O_7$ porous nanoparticles and product very active hydroxyl radicals. While O_2 acts as an electron receptor to form radical anion superoxide. Furthermore, radical superoxide anion ($^{\bullet}O_2^-$) can act as oxidizing agent or additional hydroxyl radical sources [27-29]. These active radicals are highly oxidizing and can destroy the toluene.

$$\alpha\text{-}Fe_2O_3 + h\nu \rightarrow \alpha\text{-}Fe_2O_3\,(e^-_{CB} + h^+vb) \quad (4)$$

$$h^+_{vb} + H_2O_{(ads)} \rightarrow H^+ + {}^{\bullet}OH^-_{(ads)} \quad (5)$$

$$h^+_{vb} + OH^-_{(ads)} \rightarrow {}^{\bullet}OH_{(ads)} \quad (6)$$

$$e^-_{CB} + O_{2\,(ads)} \rightarrow {}^{\bullet}O_2^-{}_{(ads)} \quad (7)$$

$$H_2O \rightleftharpoons H^+ + OH^- \quad (8)$$

$${}^{\bullet}O_2^-{}_{(ads)} + H^+ \rightarrow {}^{\bullet}HO_2 \quad (9)$$

$$2{}^{\bullet}HO_2 \rightarrow H_2O_2 + O_2 \quad (10)$$

$$H_2O_2 + \alpha\text{-}Fe_2O_3\,(e^-_{CB}) \rightarrow {}^{\bullet}OH + OH^- + \alpha\text{-}Fe_2O_3 \quad (11)$$

$${}^{\bullet}OH_{(ads)} + \text{toluene} \rightarrow \text{Degradation of toluene} \quad (12)$$

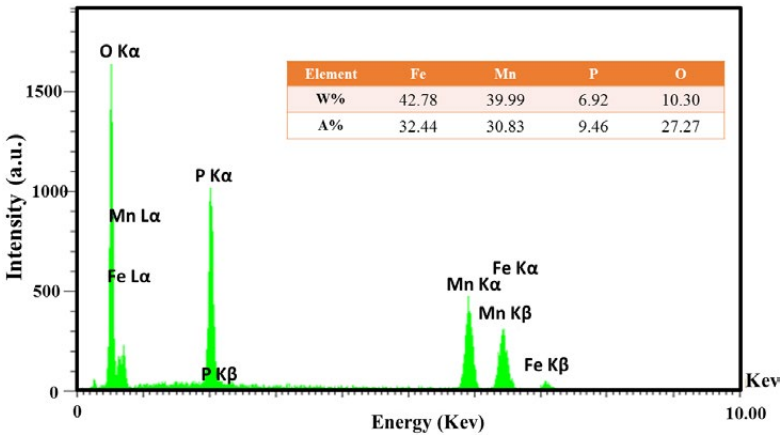

Fig. 6. The EDX spectrum of the α-Fe_2O_3/ $Mn_2P_2O_7$.

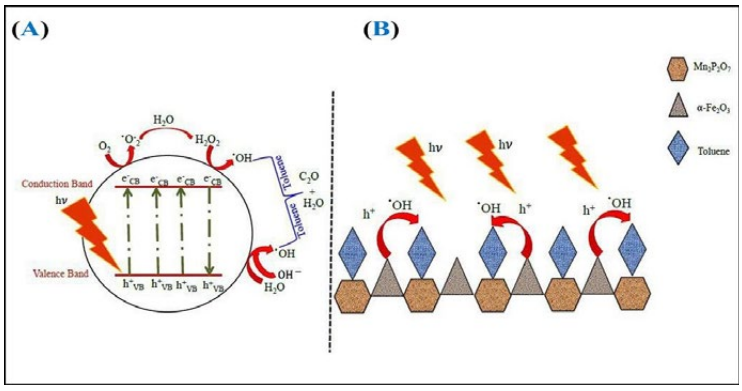

Fig. 7. The schematic of photocatalysis mechanism (A) and photocatalytic activity of α-Fe_2O_3/$Mn_2P_2O_7$ (B).

h^+vb + toluene → Oxidation of toluene (13)

With the immobilization of α-Fe_2O_3 nanoparticles on the support surface, its photocatalytic activity increases. By absorbing toluene to a larger area of support, it is more exposed to produce radicals during the photocatalytic process, thus, the degradation degree rises. The general mechanism of photocatalyst and the supportive effect on the photocatalytic enhancement of nanoparticles have been shown in Fig. 7 [30].

The effect of independent variables, namely catalyst amounts, pH, initial concentration of toluene and H_2O_2 on toluene removal were investigated. Moreover, in order to achieve the highest removal rate, the levels of the aforementioned variables were optimized. Four independent variables (each with three levels) were used in the Box-Behnken method. Independent variables for pH 5 to 9 at three levels (5, 7 and 9), H_2O_2 concentration from 0.1 to 0.5 ppm at three levels (0.1, 0.3 and 0.5 ppm), catalyst concentration from 60 to 120 ppm at three levels (60, 90 and 120 ppm) and the initial concentration of toluene from 100 to 200 ppm at three levels (100, 150 and 200 ppm), were considered (Table 1). The total number of the experiments, taking into account the test conditions, was achieved in the Box-Behnken method by 27 (Table 2).

The percentage of toluene removal was also considered as a dependent variable. The next stage involves graphically presenting the relationship between models and determining optimal operating conditions, which was done with the response and balance curve. Optimum operating conditions were searched for access to the highest amount of pollutant removal using the numerical optimization technique.

The results of ANOVA are shown in Table 3, and was used to approve the validity of models. To determine the significance of the predicted model parameters, the P-value with a 0.01 significance level is used; the smaller the p-value the more significant are the corresponding term. The effect of independent variables on toluene removal is of the order of the following: Initial concentration of toluene > catalyst concentration > H_2O_2 concentration > pH.

The information of the model should be tolerable so must have high values of R^2-adjusted and R^2-predicted. The fitting power of the model increases and the description of the response changes as a function of the independent variables increases. The R^2-adjusted to the model is 98.61% and the R^2-Predicted of the predicted model is 96.32%, these amounts indicate that the model has a very good fit and can explain the overall changes in the range of the values studied (Table 4) [31-35].

The results of the actual and predicted values are given in Table 5. As can be seen, the actual

Table 3. ANOVA results

Source	Degree of Freedom	Adj SS	Adj MS	F	P-Value
Model	14	6219.85	444.28	132.82	0.000
pH	1	53.51	53.51	16	0.002
H_2O_2 con.	1	105.91	105.91	31.66	0.000
Catalyst con.	1	541.77	541.77	161.97	0.000
Initial con. of toluene	1	4656.29	4656.29	1392.03	0.000
pH × pH	1	13.89	13.89	4.15	0.064
H_2O_2 con. × H_2O_2 con.	1	103.61	103.61	30.97	0.000
Catalyst con. × Catalyst con.	1	3.35	3.35	1	0.337
Initial con. of toluene × Initial con. of toluene	1	432.84	432.84	129.4	0.000
pH × H_2O_2 con.	1	0.01	0.01	0	0.949
pH × Catalyst con.	1	25.05	25.05	7.49	0.018
pH × Initial con. of toluene	1	67.98	67.98	20.32	0.001
H_2O_2 con. × Catalyst con.	1	39.94	39.94	11.94	0.005
H_2O_2 con. × Initial con. of toluene	1	145.32	145.32	43.45	0.000
Catalyst con. × Initial con. of toluene	1	23.81	23.81	7.12	0.020
Error	12	40.14	3.34		
Lack-of-Fit	10	39.88	3.99	30.61	0.032
Pure Error	2	0.26	0.13		
Total	26	6259.99			

and predicted values are very close together. This indicates that empirical values are close to matching the predicted values of pollutant emissions and are highly desirable for the proposed model. Mathematical model representing toluene photocatalytic decomposition in the range studied can be expressed by the following equation:

$$\begin{aligned} X\,\% &= 74.6 + 2.167(pH) + 3.182(Cat) \\ &+ 6.102(H_2O_2) - 19.88(Toluene) - 1.618(pH)^2 \\ &- 4.493(Cat)^2 + 0.977(H_2O_2)^2 - 8.928(Toluene)^2 \\ &+ 1.98(pH \times H_2O_2) - 4.122(pH \times Toluene) \\ &+ 3.137(Cat \times H_2O_2) - 5.69(Cat \times Toluene) \\ &- 2.44(H_2O_2 \times Toluene) \end{aligned} \quad (14)$$

Table 4. Compare different term effect on results.

Term	Coef	SE Coef	T (Coef/SE Coef)	P value	Result
Constant	74.67	1.06	70.71	0.000	Significant
pII	2.11	0.53	4.00	0.002	Significant
H_2O_2 con.	2.97	0.53	5.63	0.000	Significant
Catalyst con.	6.72	0.53	12.73	0.000	Significant
Toluene initial con.	-19.70	0.53	-37.31	0.000	Significant
pII × pII	-1.61	0.79	-2.04	0.064	
H_2O_2 con. × H_2O_2 con.	-4.41	0.79	-5.57	0.000	Significant
Catalyst con. × Catalyst con.	0.79	0.79	1.00	0.337	
Toluene initial con. × Toluene initial con.	-9.01	0.79	-11.38	0.000	Significant
pII × H_2O_2 con.	-0.06	0.91	-0.07	0.949	
pII × Catalyst con.	2.50	0.91	2.74	0.018	
pII × Toluene Initial con.	-4.12	0.91	-4.51	0.001	Significant
H_2O_2 con. × Catalyst con.	3.16	0.91	3.46	0.005	Significant
H_2O_2 con. × Toluene initial con.	-6.03	0.91	-6.59	0.000	Significant
Catalyst con. × Toluene initial con.	-2.44	0.91	-2.67	0.020	

S=1.83, R'=99.36%, Pred R'=96.32%, Adj R'=98.61%

Table 5. Residual values.

Exp. no.	Actual	Predict	Residual (X%-fit)	St resid
1	62.89	63.51	-0.62	-0.52
2	68.37	67.85	0.52	0.44
3	70.56	69.57	0.99	0.84
4	75.80	73.67	2.13	1.80
5	78.55	76.99	1.56	1.32
6	95.23	95.31	-0.08	-0.07
7	44.07	42.48	1.59	1.35
8	50.99	51.03	-0.04	-0.04
9	77.28	77.51	-0.23	-0.20
10	90.47	89.98	0.49	0.42
11	45.78	46.36	-0.58	-0.49
12	42.48	42.34	0.14	0.12
13	65.51	64.53	0.98	0.83
14	61.45	62.15	-0.70	-2.28
15	74.25	73.64	0.61	2.21
16	82.83	83.91	-1.08	-0.91
17	67.73	67.52	0.21	0.18
18	65.09	66.74	-1.65	-1.40
19	76.18	75.95	0.23	0.19
20	83.55	85.18	-1.63	-1.38
21	70.05	71.95	-1.90	-1.61
22	90.12	89.95	0.17	0.14
23	43.02	44.61	-1.59	-1.35
24	38.98	38.50	0.48	0.41
25	74.81	74.67	0.14	0.09
26	74.26	74.67	-0.41	-0.27
27	74.94	74.67	0.27	0.18

According to Fig. 8, the normal probability plot (a) indicates the distribution of residual values of the straight line and shows the linear pattern of compatibility with a normal distribution. The plot of residuals versus fitted values (b) has non-uniformity and does not show any particular trend. The abundance diagram of residual values (c) also indicates the relatively normal distribution of the residuals. The plot of the values remaining in relation to the observed values (d) also does not follow a particular process. Therefore, there is no systematic pattern of the residues and the fitting model is appropriate.

The results of the main effect of independent variables on pollutant removal percentage indicate that three pH, H_2O_2 and Catalyst variables had a positive and significant effect, and toluene had a negative and significant effect on the pollutant removal percentage (Fig. 9). The most effective variable was toluene concentration. The removal percentage will decrease with an increase of toluene concentration. After toluene, the catalyst was most affected. As the catalyst increased from 60 ppm to 120 ppm, the removal rate of pollutants increased significantly. The effect of pH and H_2O_2 was also positive. As the variables increased, the amount of pollutant removal increased.

The contour graphs and response surface graphs can be useful to detect the optimum conditions of the experiment. In Fig. 10 are shown the contour graph and the response 3D graph of the resulting regression model with the assumption that the concentration of the catalyst and toluene is kept constant at 90 ppm and 150 ppm, respectively. As can be seen, under the constant values of catalyst and toluene, the increase in the pH and the amount of H_2O_2 increases the efficiency of toluene removal. Therefore, if the pH ranges from 6.83 to 9 and H_2O_2 concentration ranges from 0.28 ppm to 0.46 ppm, then the amount of toluene removal would be higher than 75%, as observed.

The contour graph and the response 3D graph of the resulting regression model are shown in Fig. 11 assuming a constant H_2O_2 concentration and toluene concentration of 0.3 ppm and 150 ppm, respectively. Under the constant amounts of H_2O_2 and toluene, the efficiency of toluene removal increases with increasing pH and increasing concentration of catalyst. If the pH ranges from 6.2 to 9 and catalyst concentration ranges from 105 ppm to 120 ppm, then the amount of toluene removal would be higher than 85%.

The contour graph and the 3D response surface graph of the resulting regression model are shown

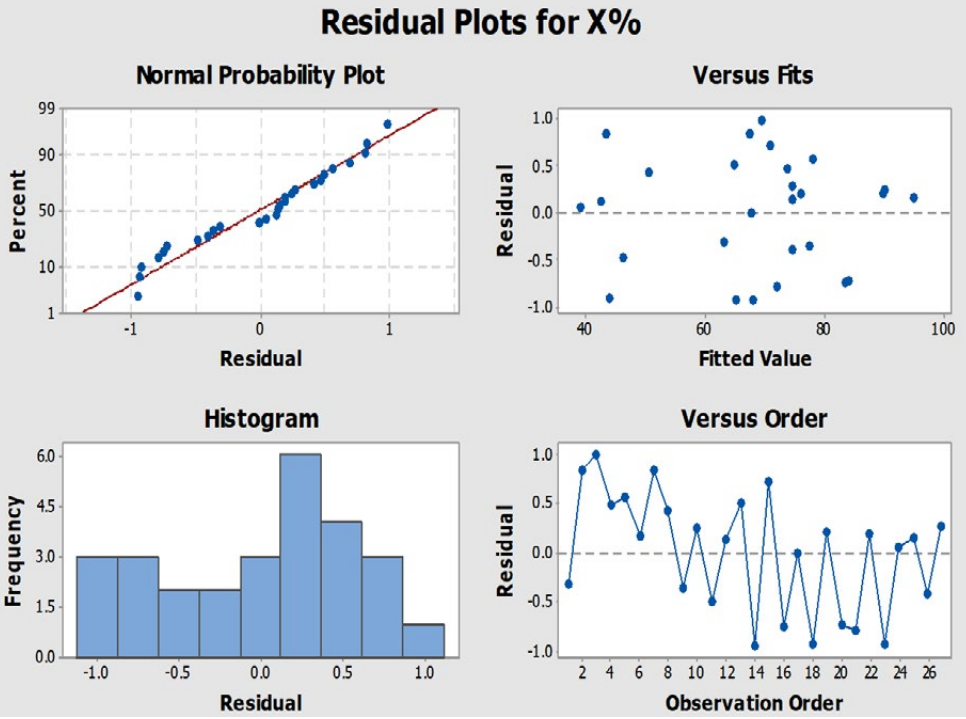

Fig. 8. Different residual plots for the photocatalytic removal of toluene from aqueous solution by the α-Fe_2O_3/$Mn_2P_2O_7$ catalyst.

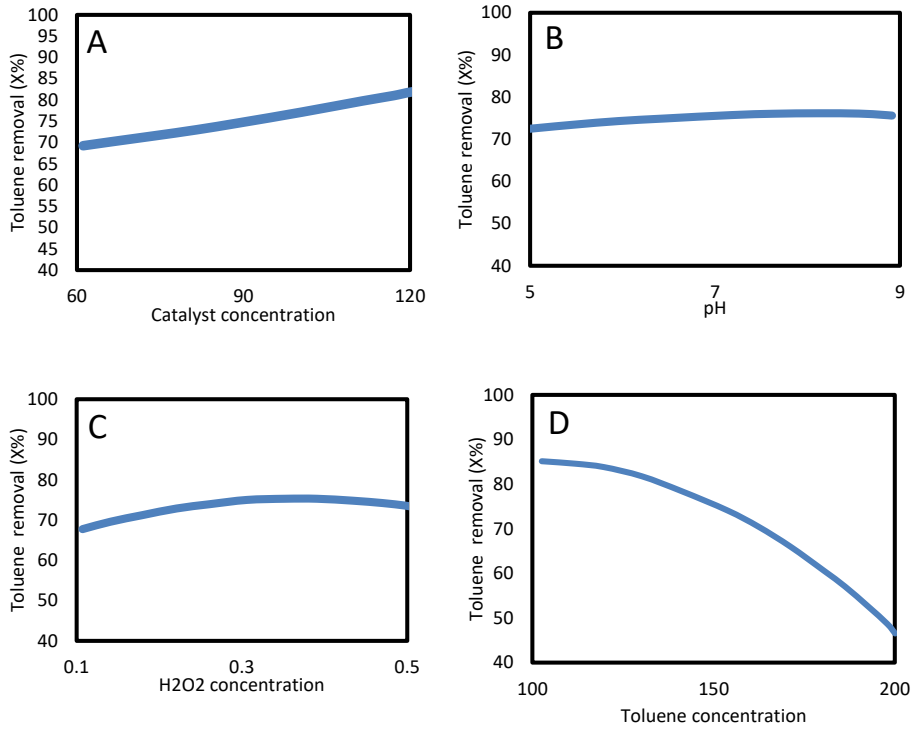

Fig. 9. The plot of variable effect on the removal percentage of toluene.

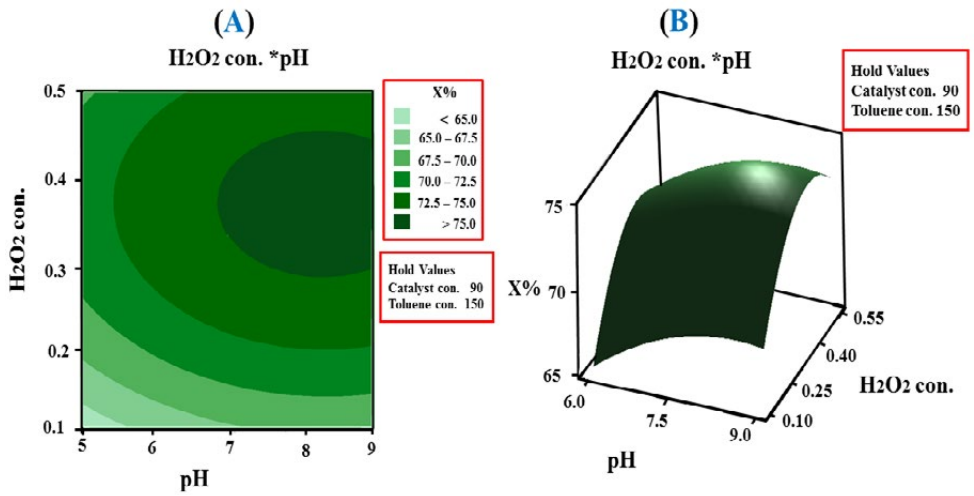

Fig. 10. Contour plots (A) and 3D Response surface (B). The interaction between pH and H_2O_2 concentration for photocatalytic toluene degradation.

Fig. 12 that assuming a constant H_2O_2 concentration and catalyst concentration in the values of 0.3 and 90, respectively under the constant values of H_2O_2 and catalyst, the efficiency of toluene removal. If the pH ranges between 8 and 9 and the concentration of toluene range between 100 ppm and 113 ppm, then the amount of toluene removal would be higher than 88%.

As shown in Fig. 13 (A) and (B), the contour graph and the 3D response surface of the resulting regression model with the assumption that the concentration of pH and toluene is kept constant at values of 7 and 150 ppm, respectively. Under the constant values of pH and toluene, increasing the amount of H_2O_2 and increasing the amount of catalyst increases the efficiency of toluene removal, so that if the H_2O_2 range is between 0.24 ppm to 0.5 ppm and the catalyst concentration is in the range

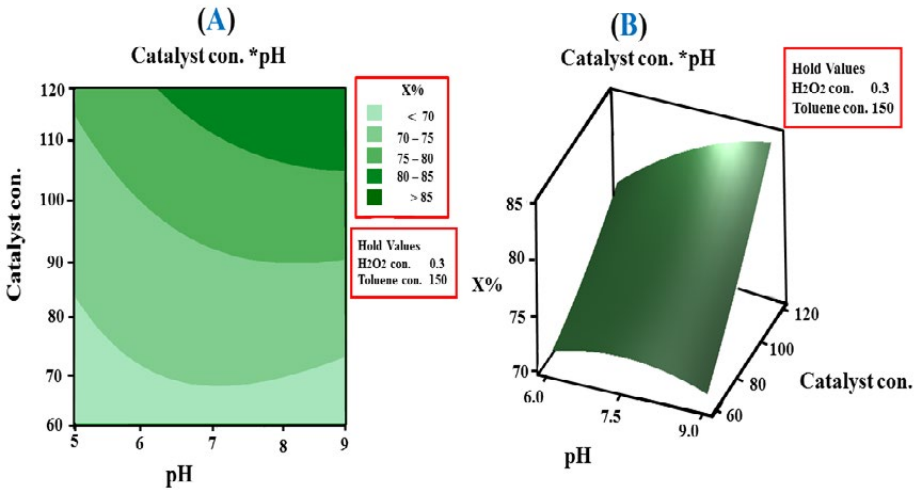

Fig. 11. Contour plots (A) and 3D Response surface (B). The interaction between pH and Catalyst concentration for photocatalytic toluene degradation.

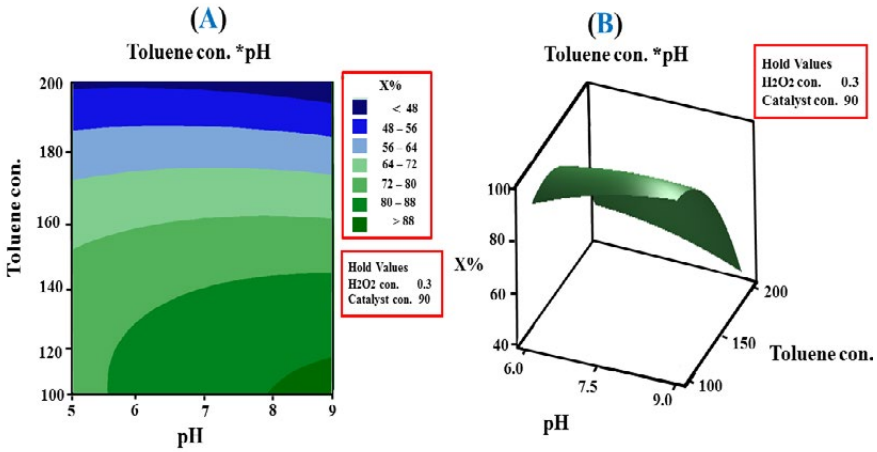

Fig. 12. Contour plots (A) and 3D Response surface (B). The interaction between pH and initial concentration of toluene for photocatalytic toluene degradation.

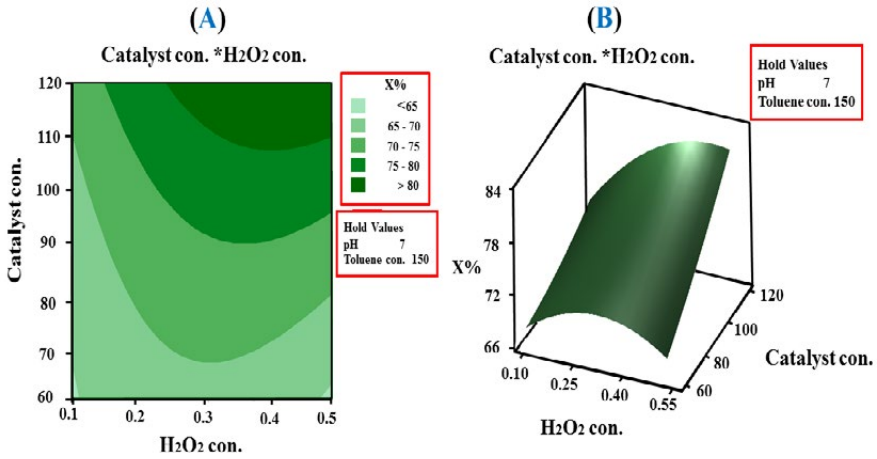

Fig. 13. Contour plots (A) and 3D Response surface (B). The interaction between H_2O_2 concentration and catalyst concentration for photocatalytic toluene degradation.

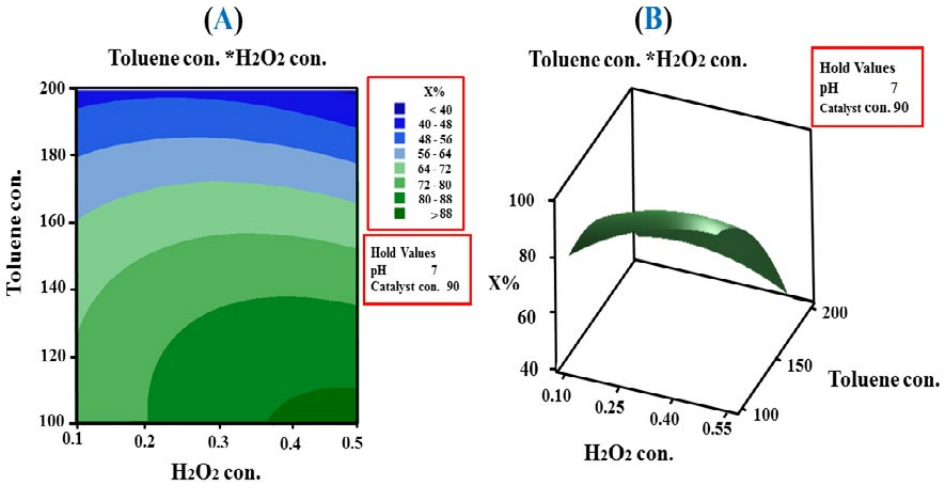

Fig. 14. Contour plots (A) and 3D response surface (B). The interaction between H_2O_2 concentration and initial concentration of toluene for toluene photocatalytic degradation.

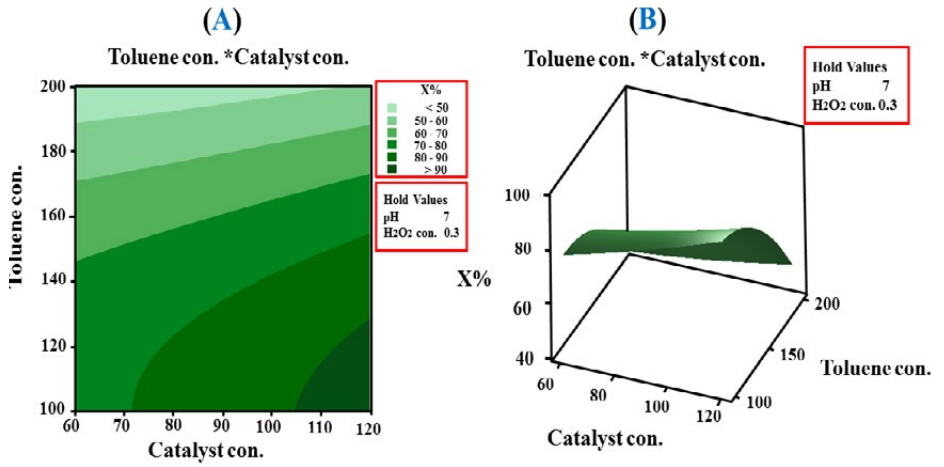

Fig. 15. Contour plots (A) and 3D Response surface (B). The interaction between Catalyst concentration and initial concentration of toluene for photocatalytic toluene degradation.

of 107 ppm to 120 ppm, the amount of toluene removal will be above 80%.

The contour graph is illustrated as Fig. 14 (A), and Fig. 14 (B) shows the 3D response of the resulting regression model with the assumption of constant pH and catalyst concentration at values of 7 and 90 ppm, respectively. Under the constant pH and catalyst concentration, increasing the amount of H_2O_2 and reducing the concentration of toluene increases the efficiency of toluene removal, so if the H_2O_2 concentration ranges from 0.37 ppm to 0.5 ppm and the catalyst concentration ranges from 107 ppm to 120 ppm, the amount of toluene removal would be higher than 88%.

With the assumption of pH=7 and H_2O_2 =0.3 ppm, the contour graph and 3D response surface graph of the resulting regression model are shown in Fig. 15 (A) and (B), respectively. Under the constant pH and H_2O_2 values, the efficiency of toluene removal increases with increasing catalyst content and decreasing toluene concentration. Accordingly, when the catalyst concentration ranges between 105-120 ppm and the toluene concentration being less than 120 ppm, then the toluene removal rate observed higher than 90%.

The exact optimal values of the variables are summarized in Table 6. As predicted, verification experiments were carried out under optimum operating conditions. The three times repeated experiments showed an average maximum of decomposition efficiency of around 97.14%. The

Table 6. Degradation analysis of toluene removal in optimum concentration and pH value.

Optimum conditions				Efficiency (%)	
pH	H_2O_2 con. (ppm)	Catalyst con. (ppm)	Toluene con. (ppm)	Predicted	Actual
8.9	0.23	120	100	98.00	97.14

proximity between the predicted and actual results approved the validity of the model and the existence of an optimum point. This proves that the RSM methodology is a powerful tool for determining the exact optimal values of the independent parameters [36-39].

CONCLUSION

In summary, the α-Fe_2O_3/$Mn_2P_2O_7$ nano photocatalyst was synthesized via the FHRC method. The physical and chemical properties of nano photocatalysts were investigated. The photocatalytic properties of the iron oxide nanoparticles have improved after fixation on the base. The results of the independent variables on toluene removal indicate that pH, H_2O_2 and catalyst have a significant effect on removal capacity, but with increased toluene initial concentration, the removal percentage was decreased. Also, at optimum conditions such as pH= 8.9, the initial concentration of toluene = 100 ppm, catalyst concentration = 120 ppm and H_2O_2 concentration = 0.23 ppm, we observed the highest percentage of toluene degradation (97.14%).

ACKNOWLEDGMENT

The authors are thankful to Islamic Azad University, Arak Branch for the preparation of experimental setup.

CONFLICT OF INTEREST

The authors declare that there is no conflict of interests regarding the publication of this manuscript.

REFERENCES

1. J. C. Sousa, A. R. Ribeiro, M. O. Barbosa, M. F. R. Pereira, A. M. Silva, J. Hazard. Mater. 344, 146 (2018).
2. M. A. Abdel-Aziz, S. A Younis, Y. M. Moustafa, M. M. H. Khalil, J. Environ. Manage. 233, 459 (2019).
3. D. Robati, S. Bagheriyan, M. Rajabi, Int. Nano Lett. 5(3), 179 (2015).
4. B. Enayatpour, M. Rajabi, O. Moradi, N. Asdolehzade, A. Nayak, S.A. garwal, V.K. Gupta, J. Mol. Liq. 254, 93 (2018).
5. A. Shokri, K. Mahanpoor, D. Soodbar, Desalination Water Treat. 1,16473(2015).
6. M. Rajabi, O. Moradi, M. Sillanpää, K. Zare, A.M. Asiri, S. Agarwal, V. K. Gupta, J .Mol. Liq. 111, 484(2019).
7. M. Rajabi, K. Mahanpoor, O. Moradi, Composites, Part B. 167, 544 (2019).
8. A. Pintar, Catal. Today. 77, 451 (2003).
9. N. Daneshvar, D. Salari, A. R. Khataee, J. Photochem. A. Photobiol. Chem. 162, 317 (2004).
10. B. Enayatpour, M. Rajabi, M. Yari, M.R. Mirkhan, F. Najafi, O. Moradi, A.K. Bharti, et al, 231, 566 (2017).
11. M. Rajabi, O. Moradi, A. Mazlomifar, Int. J. Nano Dimens. 6(3), 227 (2015).
12. N. Daneshvar, M. Rabbani, N. Modirshahla, M. A. Behnajady, J. Photochem. A. Photobiol. Chem. 168, 39 (2004).
13. S. Khodadoost, A. Hadi, J. Karimi-Sabet, M. Mehdipourghazi, A. Golzary, J. Environ. Chem. Eng. 5, 5369 (2017).
14. M. Yari, M. Norouzi, A.H Mahvi, M. Rajabi, A. Yari, O. Moradi, I. Tyagi, V.K. Gupta, Desalin. Water Treat. 57(24), 11195 (2016).
15. Y. I. Choi, K. H. Jeon, H. S. Kim, J. H. Lee, S. J. Park, J. E. Roh, Y. Sohn, Sep. Purif . Technol. 160, 28 (2016).
16. M. Mishra, D. M. Chun, Appl. Catal. 498, 126 (2015).
17. T. J. Greenfield, M. Julve, R. P. Doyle, Coord. Chem. Rev. 384, 37 (2019).
18. S. Wang, X. Jiang, G. Du, Z. Guo, J. Jang, S. J. Kim, Mater. Lett. 65, 3265 (2011).
19. M. Saghi, K. Mahanpoor, H. Shafiei, Iran. J. Chem. Chem. Eng. Research Article. 37,1 (2016).
20. N. Tafreshi, S. Sharifnia, S. Moradi Dehaghi, Process. Saf. Environ. Prot. 106, 203 (2017).
21. E. Ambrosio, D. L. Lucca, M. H. Garcia, R. P. de Souza, J. V. Visentainer, D.L. Lucca, , J. C. Garcia, et al, Sci. Total. Environ. 581, 1 (2017).
22. D. Robati, S. Bagheriyan, M. Rajabi, O. Moradi, A. Ahmadi Peyghan, Phys. E, 83, 1 (2016).
23. S. N. Nam, H. Cho, J. Han, N. Her, J. Yoon, Process. Saf. Environ. Prot. 113, 10 (2018).
24. B. Boonchom, R. Baitahe, Mater. Lett. 63, 2218 (2009).
25. M. Chen, J. Liu, D. Chao, J. Wang, J. Yin, J. Lin, Z. X. Shen, Nano. Energy. 9, 364 (2014).
26. A. Lassoued, B. Dkhil, A. Gadri, S. Ammar, Results. Phys. 7, 3007 (2017).
27. O. Mehraj, B. M. Pirzada, N. A. Mir, M. Z. Khan, S. Sabir, Appl. Surf. Sci. 387, 642 (2016).
28. M. Rajabi, B. Mirza, K. Mahanpoor, M. Mirjalili, F. Najafi, O. Moradi, H. Sadegh, et al, Ind. Eng. Chem. 34, 130 (2016).
29. D. Zhao, G. Sheng, C. Chen, X. Wang, Appl. Catal. B. Environ. 111, 303 (2012).
30. V. Augugliaro, M. Bellardita, V. Loddo, G. Palmisano, L. Palmisano, S. Yurdakal, J. Photochem. Photobiol. C. Photochem. Rev. 13, 224 (2012).
31. O. Mehraj, B. M. Pirzada, N.A. Mir, M.Z. Khan, S. Sabir, Appl. Surf. Sci. 387, 642 (2016).
32. A. Shokri, K. Mahanpoor, D. Soodbar, Fress Environ Bull.

25(2), 500 (2016).
33. D. Robati, M. Rajabi, O. Moradi, F. Najafi, I. Tyagi, S. Agarwal, V.K. Gupta, J. Mol. Liq. 214, 259 (2016).
34. A. Lassoued, B. Dkhil, A. Gadri, S. Ammar, Results. Phys. 7, 3007 (2017).
35. D. Robati, B. Mirza, M. Rajabi, O. Moradi, I. Tyagi, S. Agarwal, V.K. Gupta, Chem. Eng. J. 284, 687 (2016).
36. A. Shokri, F. Rabiee, K. Mahanpoor, Int. J. Environ. Sci. Technol. 14, 2485 (2017).
37. M. Rajabi, K. Mahanpoor, O. Moradi, J. Appl. Polym. Sci. 136(22), 47495 (2019).
38. A. Shokri, K. Mahanpoor, D. Soodbar, J. Environ. Chem. Eng. 4, 585 (2016).
M Rajabi, O Moradi, K Zare, Int. Nano Lett.7(1), 35 (2017).